

Manuscript prepared for Atmos. Chem. Phys. Discuss.
with version 2.0 of the L^AT_EX class copernicus_discussions.cls.
Date: 16 December 2009

Downscaling of METEOSAT SEVIRI 0.6 and 0.8 micron channel radiances utilizing the high-resolution visible channel

Hartwig Deneke^{1,2} and Rob Roebeling¹

¹ Royal Netherlands Meteorological Institute, Postbus 201, 3730 AE De Bilt, the Netherlands

² Meteorological Institute, University of Bonn Auf dem Hügel 20, 53121 Bonn, Germany

Correspondence to: Hartwig M. Deneke
(hartwig.deneke@gmail.com)

Abstract

An algorithm is introduced to downscale the 0.6 and 0.8 micron spectral channels of the METEOSTAT SEVIRI satellite imager from $3 \times 3 \text{ km}^2$ (LRES) to $1 \times 1 \text{ km}^2$ (HRES) resolution utilizing SEVIRI's high-resolution visible channel (HRVIS). Intermediate steps include the coregistration of low- and high-resolution images, lowpass filtering of the HRVIS channel with the spatial response function of the narrowband channels, and the estimation of a least-squares linear regression model for linking high-frequency variations in the HRVIS and narrowband images. The importance of accounting for the sensor spatial response function for matching reflectances at different spatial resolutions is demonstrated, and an estimate of the accuracy of the downscaled reflectances is provided. Based on a 1-year dataset of Meteosat SEVIRI images, it is estimated that on average, the reflectance of a HRES pixel differs from that of an enclosing LRES pixel by standard deviations of 0.049 and 0.052 in the 0.6 and 0.8 micron channels, respectively. By applying our downscaling algorithm, explained variance of 98.2 and 95.3 percent are achieved for estimating these deviations, corresponding to residual standard deviations of only 0.007 and 0.011 for the respective channels. **For this dataset, a minor misregistration of the HRVIS channel relative to the narrowband channels of $0.36 \pm 0.11 \text{ km}$ in East and $0.06 \pm 0.10 \text{ km}$ in South direction is observed and corrected for, which should be negligible for most applications.**

1 Introduction

Accurate information on cloud properties is a prerequisite for understanding the influence of clouds on the Earth radiation budget and the global hydrological cycle. Due to their dominant role as forcing of the surface energy budget, accurate information on surface radiative fluxes in cloudy conditions is of particular interest (Woods et al., 1984; Wielicki et al., 1995). Passive meteorological satellite imagers provide important information for investigating cloud properties (Stephens and Kummerow, 2007), and for

quantifying their influence on solar (Deneke et al., 2005) and thermal (Schmetz et al., 1990) radiation. Several projects generate data records of cloud properties, including the International Satellite Cloud Climatology Project (ISCCP, Rossow and Schiffer, 1991), the Pathfinder Atmospheres project (PATMOS, Jacobowitz et al., 2003), the MODIS project (Platnick et al., 2003), and the Satellite Application Facility on Climate Monitoring (CM-SAF, Schulz et al., 2009).

Geostationary imagers such as the Spinning Enhanced Visible Radiometer (SEVIRI, Schmetz et al., 2002) are unique in their capability to fully resolve the diurnal cycle of clouds (e.g., Roebeling and van Meijgaard, 2008). However, the nadir spatial sampling resolution of $3 \times 3 \text{ km}^2$ offered by SEVIRI's narrowband channels lags significantly behind that of polar-orbiting satellite imagers (e.g., AVHRR with $1.1 \times 1.1 \text{ km}^2$ or MODIS down to $0.25 \times 0.25 \text{ km}^2$). Due to the highly nonlinear relationship between radiances and cloud properties, differences in sensor resolution can cause large random and systematic differences in cloud properties such as optical thickness and liquid water path (Oreopoulos and Davies, 1998; Deneke et al., 2009b), and causes uncertainties classification of cloud thermodynamic phase (Wolters et al., 2009). In addition, the considered spatial (Greuell and Roebeling, 2009; Schutgens and Roebeling, 2009) and temporal (Deneke et al., 2009a) scales of variability have a strong impact on the correspondence of satellite and ground observations, and thus the task of satellite product validation.

Moreover, the spatial resolution of SEVIRI's narrowband channels is insufficient to resolve small cloud structures. As demonstrated by Heidinger and Stephens (2001), unresolved spatial heterogeneity can cause errors in retrieved cloud properties large enough to render them useless. To partly overcome this problem, Klüser et al. (2008) utilized the high-resolution broadband visible channel (HRVIS) with a sampling resolution of $1 \times 1 \text{ km}^2$ at nadir to study the lifecycle of shallow convective clouds.

There are two important drawbacks of the HRVIS channel: first, it covers only a subset of the field of view of the narrowband channels; second, its spectral response is too broad for an accurate quantitative estimation of cloud properties. While there

is little to be done about the first point, the purpose of this paper is to overcome the second point.

Cros et al. (2006) have demonstrated that the relationship between reflectances from SEVIRI's 0.6 and 0.8 micron channels and the MVIRI (Meteosat Visible and InfraRed Imager) broadband visible channel onboard Meteosat-7 (Meteosat First Generation) is highly linear and stable in time, due to the spectral overlap of these channels. Since the MVIRI channel of Meteosat First Generation and the HRVIS channel of Meteosat Second Generation have very similar spectral responses (Schmetz et al., 2002), their finding should also hold for the HRVIS channel, and indicates that the variations observed in the HRVIS reflectances will be strongly correlated to those observed in the 0.6 and 0.8 micron channel.

The goal of Cros et al. (2006) was to predict the broadband channel reflectance from the narrowband channels so as to generate input for legacy applications based on MVIRI. In contrast, the purpose of this paper is to introduce a novel algorithm to estimate the reflectances of the 0.6 and 0.8 micron channels at the threefold higher spatial resolution of the HRVIS channel, by utilizing the HRVIS reflectances as predictor. As constraint, the statistical properties of the narrowband reflectances should be preserved at their native channel resolution. Such methods are referred to as downscaling (Liu and Pu, 2008) in climate research or disaggregation (Walker and Mallawaarachchi, 1998) in geostatistics. Following Cros et al. (2006), we have decided to use image-wide linear models for simplicity, and neglect any scene-type dependencies. Other SEVIRI narrowband channels apart from 0.6 and 0.8 micron are ignored at the moment. This work nevertheless constitutes a first step towards producing higher spatial resolution products from SEVIRI such as cloud water path (e.g., Roebeling et al., 2008) and solar surface irradiance (e.g., Deneke et al., 2008; Müller et al., 2009) over Europe.

In this paper, special attention is paid to some technical details which might affect the quality of our proposed algorithm. First, the spatial response of the SEVIRI channels does not correspond to the idealized form of a rectangular function, and the radiance field is significantly oversampled, as has been pointed out

by Schmetz et al. (2002). This causes radiance contributions from a region significantly larger than the $3 \times 3 \text{ km}^2$ sampling resolution (referred to as LRES in the following) of the narrowband channels, and the $1 \times 1 \text{ km}^2$ resolution of the HRVIS channel (referred to as HRES). Thus, it is insufficient to use simple arithmetic averages of $3 \times 3 \text{ km}^2$ pixels to reduce the resolution of the HRVIS images to that of the narrowband channels, and the true sensor spatial response should be used instead. In addition, an accurate coregistration of the LRES channels with the HRVIS channel is crucial for the quality of our downscaling scheme. As Dürr and Zelenka (2008) and Dürr et al. (2009) report systematic biases in the navigation of the HRVIS channel, we have decided to investigate the accuracy of the image coregistration. Our algorithm uses frequency-domain methods based on the discrete Fourier transform for modeling the spatial response function of SEVIRI's detectors (Markham, 1985) and to determine the image coregistration (Anuta, 1970). These methods have the advantage of being both mathematically elegant and computationally efficient.

This paper is structured as follows. In Sec. 2, the instrumental dataset is described. An outline of the proposed downscaling algorithm is given in Sec. 3, with some general background provided as Appendices. In Sec. 4, examples of results obtained with these methods are reported, and the accuracy of our method is demonstrated and discussed. Finally, conclusions and an outlook are given in Sec. 5.

2 Instrumental Data

Meteosat Second Generation is the current series of European geostationary satellites, which began operational data acquisition in January 2004 and is described in detail by Schmetz et al. (2002). Its Meteosat-8 and 9 satellites carry the SEVIRI imager as primary instrument, and are positioned above the equator at longitudes of 0.0°W and 9.6°E , respectively, at the time of writing. In operational service, the SEVIRI imager scans the complete disk of the earth with a 15 minute repeat cycle. Meteosat-9 is cur-

rently the operational satellite, while Meteosat-8 is used as hot stand-by, and scans a subregion with a 5 minute repeat cycle in Rapid Scan Mode. SEVIRI has 3 narrow-band solar channels (0.6, 0.8 and 1.6 micron), the broadband HRVIS channel (0.3-1.1 micron), and 8 thermal infrared channels (3.9, 6.2, 7.3, 8.7, 9.7, 10.8, 12.0 and 13.4 micron).

Only the 0.6 and 0.8 micron channels, and the HRVIS channel are considered in this study. Their spectral response functions are shown in Fig. 1 for the Meteosat-9 instrument, while parameters characterizing their spectral characteristics are listed in Tab. 1 for Meteosat-8 to 10. The SEVIRI imager acquires pixels at sampling resolutions of $1 \times 1 \text{ km}^2$ and $3 \times 3 \text{ km}^2$ for the high-resolution visible channel (HRVIS) and the narrowband channels, respectively. It has to be realized, however, that SEVIRI has a lower optical resolution and oversamples the reflectance field by a factor of about 1.6 at both LRES and HRES resolution (Schmetz et al., 2002). Thus, the effective area contributing to an individual pixel radiance is significantly larger than the sampling resolution. This is illustrated in Fig. 2b, which displays the response of the SEVIRI detectors to a unit pulse of radiance as function of distance from the pixel center, and shows significant contributions from regions outside the nominal sampling resolution. Its calculation is explained in Sec. 3.3

3 Methodology

This section presents our proposed downscaling algorithm. In overview, it consists of the following sequence of steps:

1. coregistration of the HRVIS and the narrowband images to ensure an optimal alignment of the satellite images;
2. Filtering of the HRVIS image with the spatial response function of the LRES detectors, to separate the image into low-frequency variability resolved at LRES scale, and unresolved high-frequency variability;

3. Determination of a least-squares linear model based on LRES reflectances to link the HRVIS, 0.6 and 0.8 micron channels as proposed by Cros et al. (2006);
4. Inversion of the linear model found in step 3 to determine estimates of the high-frequency variations in the 0.6 and 0.8 micron images using the HRVIS high-frequency variability from step 2 as predictor; least-squares estimators are used to overcome the underconstrained nature of this inversion;
5. trigonometric interpolation of the 0.6 and 0.8 micron channels to obtain images at HRES resolution, but lacking high-frequency variability;
6. addition of high-frequency variability found in step 4 to the 0.6 and 0.8 micron HRES images as estimate of the true HRES image;

More details about these steps are described in the following. A brief summary of the Fourier Transform is given first. Then, its application to the tasks of image coregistration, and to the separation of low- and high-frequency spatial variations is described. Next, the determination of a linear model for linking the $0.6 \mu\text{m}$, $0.8 \mu\text{m}$ and HRVIS radiances, and for inverting this model is outlined, in order to estimate the unresolved variability in the narrowband channels. Finally, some implementation details are noted.

3.1 The Fourier transform

The discrete Fourier transform $\hat{f}_{k,l}$ of a 2D image $f_{x,y}$ consists of $N_x \times N_y$ samples, and projects the original image onto an orthonormal basis set of sinusoidal waves with circular frequencies of $\omega_k = \frac{2\pi k}{N_x}$, $k \in 0 \dots (N_x - 1)$ and $\omega_l = \frac{2\pi l}{N_y}$, $l \in 0 \dots (N_y - 1)$. Vectors ω and x can be used to compactly represent the 2-dimensional case of the Fourier transform.

Fourier analysis implicitly treats signals as periodic. To avoid the influence of resulting discontinuities at the edges, it is common practice to subtract the mean and to use a window function to reduce the deviations from zero at the edges of the image prior

to the Fourier transform. Here, the Tukey window with a transition width of 25 percent along both dimension is used. A detailed discussion of window functions and their relevance for Fourier analysis can be found in Harris (1978).

3.2 Image coregistration

- 5 Our approach for image coregistration relies on the so-called Fourier shift theorem: the Fourier transform of a function $f'(x) \equiv f(x - x_0)$ shifted by an offset x_0 versus the original function f is given by

$$\widehat{f'}(\omega) = \widehat{f}(\omega) \exp[i\omega x_0]. \quad (1)$$

- 10 Thus, the translation of a function changes only the complex phase of its Fourier transform, while leaving its amplitude invariant. To align a satellite image g relative to an image f , a function h is defined as follows:

$$h \equiv \widehat{g} \widehat{f}^* = \|\widehat{g}\| \|\widehat{f}\| \exp[i(\arg(\widehat{g}) - \arg(\widehat{f}))]. \quad (2)$$

Here, the \arg operator determines the phase of a complex number. If $g(x) = f(x - x_0)$, $\arg(h)$ will only depend on the shift x_0 according to

$$15 \arg(h) = \arg(\widehat{g}) + \omega x_0 - \arg(\widehat{f}) = 2\pi \left[\frac{k}{N_x} x_0 + \frac{l}{N_y} y_0 \right] \quad (3)$$

- In our case, the complex phase of h is calculated from the Fourier transforms of the HRVIS and the narrowband images for individual SEVIRI scenes. A linear combination of the 0.6 and 0.8 image is used for this purpose, as is explained in Sec. 3.4. Fourier coefficients of the HRVIS image beyond the Nyquist frequency of the LRES images are
 20 ignored. Theoretically, Eq.3 suggests a perfect linear relation. In practice, deviations from this equation are expected due to image differences and the discrete sampling. A 2-dimensional linear least-square regression of Eq.3 nevertheless provides a reliable and accurate estimate of the image shifts x_0 and y_0 . As noise introduces larger phase

errors for complex numbers with small modulus, a weighted linear regression is used here with the modulus used as weight. Once the shift has been found, the HRVIS image is aligned to the narrowband images by multiplying its Fourier transform with the complex factor $\exp[-i\omega\mathbf{x}_0]$. It should be noted that this method is thus able to correct even for a fractional shift of the pixel resolution.

3.3 Spatial response of a detector

To separate high-frequency variability not resolved at LRES scale from low-frequency variability in the HRVIS channel, the effects of the spatial response function of the LRES detectors need to be considered.

We assume that the signal S of an individual SEVIRI pixel can be determined by spatial integration of the radiance $L(\mathbf{x})$ reflected from the earth surface at location \mathbf{x} , weighted by a function $w(\mathbf{x} - \mathbf{x}_0)$ which characterizes the spatial response of the detector:

$$\begin{aligned} S(\mathbf{x}_0) &= \int_A w(\mathbf{x} - \mathbf{x}_0) L(\mathbf{x}) d\mathbf{x} \\ &= (w * L)(\mathbf{x}_0). \end{aligned} \tag{4}$$

Here, \mathbf{x}_0 is the displacement from the center of the detector field of view. The weighting function w is commonly referred to as point spread function. We require w to be non-zero only in a finite region A around the pixel center, and to be normalized to the area of this region. The latter condition ensures that S corresponds to a spatially weighted mean of the radiance. Eq.4 neglects internal feedbacks in the detector, and characterizes its output as a class of digital filters known as finite-impulse response (FIR) filters in signal processing. In principle, it is possible to determine w by moving a point source of unit radiance across the detector field of view. In the second line of Eq.4, the symbol $*$ denotes the convolution of two functions. To evaluate this convolution efficiently, the Fourier convolution theorem can be used, which states that the convolution in spatial domain is equivalent to a multiplication in frequency domain. Hence, the impact

of a detector's spatial response on scene sampling can be accounted for by a simple multiplication of the Fourier transforms of L and w .

The modulus of the Fourier transform of w is called the modulation transfer function (MTF), and describes the ratio of the amplitudes of a sinusoidal wave before and after passing through an optical system. The MTF is thus a commonly used quantity to characterize the spatial resolution of optical systems. Fig. 2a displays the average MTFs of Meteosat-9 SEVIRI's 0.6, 0.8 micron and HRVIS channels as reported by EUMETSAT (2006a). As the MTF of the narrowband channels differ only slightly, they have been averaged, and any deviations between the two channels and individual detectors are neglected. The figure also illustrates the difference in spatial response in North-South and East-West direction. In Fig. 2b, the point spread function w is shown, which has been calculated from the MTF by the inverse Fourier transform. Even symmetry about the origin has been assumed for w to ensure that both w itself and its Fourier transform are real functions. This makes w a zero-phase FIR filter, a property which implies that the original and the filtered image remain unshifted relative to each other.

In our downscaling algorithm, the HRVIS image is filtered with the MTF as low-pass filter to simulate an LRES image. This filtering operation is carried out in the frequency domain by multiplication of the Fourier transform with the MTF. High-frequency variability not resolved by the LRES images is then found as difference of unfiltered and filtered HRVIS image.

3.4 Linear Relation of Channel Radiances

Our paper builds upon the study of Cros et al. (2006). Based on collocated satellite images from Meteosat-7 and Meteosat-8, they have demonstrated that SEVIRI's 0.6 and 0.8 micron channel radiances can be used in a linear model to predict the broadband solar channel of the MVIRI instrument onboard Meteosat-7 with high accuracy. They motivate this assumption with the overlap of the narrowband channels and the MVIRI broadband channel. As the spectral response of SEVIRI's HRVIS channel is similar to

the MVIRI broadband solar channel (Schmetz et al., 2002), we also adopt this assumption. Instead of radiances, however, the LRES reflectances of the 0.6 micron (r_{06}), 0.8 micron (r_{08}), and the HRVIS (r_H) channels are used here in the linear model:

$$r_H = a r_{06} + b r_{08}. \quad (5)$$

5 In this equation, a and b are fit coefficients determined by least-squares linear regression. No offset is incorporated into the linear model, as it has been found to cause only a negligible improvement in model quality.

For a formal look at the arguments of Cros et al. (2006), the channel center and width, as well as similar quantities weighted by the extraterrestrial solar spectrum are defined in Appendix A to characterize the spectral response function η of a satellite detector. Fig. 1 graphically displays these quantities for the SEVIRI instrument on Meteosat-9, while numerical values as reported by (EUMETSAT, 2006b) are listed in Tab. 1 for Meteosat-8, 9 and 10. Both narrowband channels lie completely within the range of the HRVIS channel. Weighting by the solar spectrum reduces the width of all channels, and shifts the channel centers towards the maximum of the solar spectrum. Both effects are most pronounced for the HRVIS channel due to its large width.

15 These numbers also reveal that both narrowband channels cover less than a third of the solar energy contained in the spectral range of the HRVIS channel. Hence, channel overlap is only a partial explanation of the high accuracy of the linear model reported by Cros et al. (2006). A high degree of autocorrelation of the reflectances across the spectral region of the HRVIS channel is thus also required. This spectral autocorrelation also ensures that the results presented here are relatively insensitive to the width of the narrowband channels of the SEVIRI instrument, and motivates our choice of reflectance instead of radiance as variables in Eq.5.

25 **3.5 Estimation of unresolved variability**

In contrast to Cros et al. (2006), our aim is to estimate high-frequency variations in both narrowband channels from corresponding HRVIS variations, by inversion of Eq.5.

Mathematically, it is impossible to determine two unknowns from one linear equation, as this is an underconstrained problem. Due to a strong correlation of the 0.6 and the 0.8 micron channel, an accurate estimate can nevertheless be obtained using standard least-squares estimators.

5 In Appendix B, general formulae are derived for calculating the slope (Eq.B6) and the expected fraction of explained variance (Eq.B8) of the linear model minimizing the least-squares deviations based on fundamental relations of bivariate statistics are derived. Both formulae depend only on the coefficients a and b from Eq.5, the correlation between the 0.6 and 0.8 micron reflectance, and the ratio of the variances of both
10 channels. It has to be recognized, however, that these parameters might vary with the spatial scale of variability, and that we require their values at HRES scale here, which is not available from SEVIRI. To still obtain an estimate of their value, and to minimize errors caused by scale mismatch, both parameters are calculated considering the smallest resolved scale of variability present in the LRES images. For the pur-
15 pose of parameter estimation, we thus use difference images obtained by subtracting a shifted from an unshifted image, with shifts of 1 pixel applied in both the North-South and East-West direction. This procedure corresponds to a highpass filter, with maximum filter response at the Nyquist frequency of the LRES images, which is half the sampling frequency, and thus the maximum frequency captured in the LRES images.

20 **3.6 Implementation Details**

At the beginning of this section, the sequence of steps comprising the downscaling algorithm has been listed. In practise, the individual steps of our implementation are not independent as suggested by that list. As first step, the HRVIS image is shifted relative to the narrowband channels to account for misregistration. As reference, the
25 linear combination of the 0.6 and 0.8 micron channel given by Eq.5 is used. The required coefficients are only found in step 3, however. In addition, it is more accurate to account for integer HRVIS pixel shifts by changing the subregion of the HRVIS image instead of adding a phase shift to the Fourier transform.

Therefore, mean values of the linear weights and pixel shifts are used initially, and steps 1 to 3 are carried out iteratively until the remaining image misregistration is smaller than half a HRVIS pixel size. Most of the time, this condition is met already by the first iteration.

5 4 Results and Discussion

In this section, results of the proposed downscaling algorithm are presented, and several aspects relevant to the accuracy of the algorithm are discussed.

A sub-region containing 1024×512 LRES pixels from SEVIRI's field of view has been selected for our study, which is shown in Fig. 3. It covers Northern Africa, the Mediterranean Sea, and a large part of Europe. A smaller number of pixels in North-South than in East-West direction is used to limit the change in pixel resolution caused by the increase of satellite viewing angle away from the equator. The Tukey window function applied to the data prior to the Fourier transform is also shown by red contours, which corresponds to a cosine-shaped transition from 0 to 1 over 64 LRES pixels at the Northern and Southern edges, and 128 LRES pixels at the Eastern and Western edge, respectively. One year's worth of satellite scenes acquired at 12:00 UTC during 2008 has been analyzed. This yields a total number of 345 scenes from Meteosat-9, and 10 scenes acquired by Meteosat-8 operating as backup during satellite anomalies of Meteosat-9. The remaining 10 scenes are missing or corrupted in KNMI's archive.

Fig. 4 shows the English channel and the Benelux states as example output in a SEVIRI scene acquired at 12:00 UTC on June 26th, 2008. This subregion is marked in Fig. 3 by a black shaded rectangle. Panel (a) displays this scene in grey scales as observed by the HRVIS channel. Panel (b) shows the same scene using the *day natural color* false-color composite described in detail by Lensky and Rosenfeld (2008) at LRES resolution. This scheme uses the 1.6, 0.8 and 0.6 micron spectral channels as red, green, and blue signals, respectively, and facilitates the physical interpretation of the image, as it allows to easily distinguish different surface types, as well as ice and

water clouds. Panel (c) shows this scene once more using the color scheme of (b), but based on the downscaled 0.6 and 0.8 micron spectral channels (the resolution of the 1.6 micron channel has been increased to HRES by sinc interpolation).

During that day, a high pressure ridge extended from the Azores over France and Germany with moderate summer temperatures and relatively dry air, and temporarily replaced hot and humid air masses. A low pressure system was located to the North of the British Isles. The satellite scene shows scattered fair-weather cumuli over South-Eastern England and mainland Europe. A large cirrus cloud over the North Sea can be recognized by its typical blue color, which is due to the low reflectance in the 1.6 μm channel caused by ice absorption (Knap et al., 2002). While the LRES day natural color composite in panel (b) misses a lot of the spatial structures visible in the HRVIS image, it allows a much easier interpretation of the image due to its use of multi-spectral information. Visually, panel (c) clearly demonstrates that our downscaling scheme is able to combine the advantage offered by the day natural color composite with the higher spatial resolution of the HRVIS channel. It could therefore become a valuable tool for assessing the synoptic situation in operational weather forecasting environments.

While these qualitative results are encouraging, a proper uncertainty analysis is required to judge the suitability of the downscaled reflectances as input for quantitative satellite retrievals. For this purpose, two separate sources of uncertainty are considered, which are assumed to be statistically independent. The first source results from deviations from the linear model between the 0.6, 0.8 micron and HRVIS reflectance given by Eq.5. The second source of uncertainty lies in the underconstrained nature of the downscaling problem, which has been discussed in Sec. 3.5 and is quantified by Eq.B8. Average values of the required parameters have been calculated for the entire dataset and are listed in Tab. 2.

As measure of uncertainty, the fraction of unexplained variance UV is considered, which is related to the explained variance EV by $UV = 1 - EV$. Assuming independent error propagation, the combined fraction of unexplained variance is given as the sum of the two individual fractions of unexplained variance. Calculating the total unresolved

variability based on the values given in Tab. 2, values of 1.8% and 4.7% are found, with corresponding values of total explained variance of 98.2% and 95.3% for the 0.6 and 0.8 micron channels, respectively. Looking at the relative contributions to the uncertainty, fractions of 80.6% and 91.6% are attributable to the inversion carried out by Eq.B6, and identifies it as the dominating source of uncertainty. The uncertainty is larger for the 0.8 micron than for the 0.6 micron channel, as its influence on the HRVIS channel is smaller, as is indicated by the value of b being smaller than a in Eq.5.

Fig. 5a displays the annual time series of the slopes $S(r_{06})$ and $S(r_{08})$ calculated for individual satellite scenes. To relate the fraction of unexplained variance to an estimate of the absolute accuracy of the downscaling algorithm, the increase in variance going from LRES to HRES resolution is needed. It is expressed as standard deviation by use of the square root of the variance here. Fig. 5b shows annual time series for the 0.6, 0.8 micron and HRVIS channels. The 0.6 and 0.8 micron values are estimated from the HRVIS values using the slopes $S(r_{06})$ and $S(r_{08})$, and applying the general property of the variance that $\text{Var}(ax) = a^2 \text{Var}(x)$ for a constant a and a random variable x . Panel Fig. 5c plots the time series of the expected residual standard deviation of the downscaled and true HRES images, based on the estimate of unresolved variability outlined in the previous paragraph.

Panel a of Fig. 5 shows that on average, the narrowband reflectances of a HRES pixel within the $3 \times 3 \text{ km}^2$ sampling resolution of a LRES pixel deviates from the LRES reflectance by absolute amounts of 0.049 and 0.051 for the 0.6 and 0.8 micron images, respectively. This variability is not taken into account if only the LRES images are used. By applying our downscaling algorithm, we are able to reduce these deviations to values of only 0.007 and 0.011.

In the introduction, we have argued that the effects of sensor spatial response and image misregistration will affect the accuracy of the proposed downscaling scheme. To support this argument, the resulting improvements reflected in the mean value of explained variance for the linear model Eq.5 are reported in Tab. 3. As reference, the value obtained by our proposed algorithm as described

in Sec. 3.4 is used. Four alternative filtering strategies have been tested to obtain LRES images from the HRVIS channel. Denoted by LP48, all Fourier coefficients with a frequency above $0.5 \times 4.8^{-1} \text{ km}^{-1}$ were set to zero in the filtering process, corresponding to a perfect lowpass filter for the $4.8 \times 4.8 \text{ km}^2$ resolution reported by Schmetz et al. (2002). An alternative is the use of arithmetic averaging of a neighborhood of pixels. Here, square regions consisting of 1×1 , 3×3 pixels and 5×5 pixels were considered. The values given in the table support that accounting for the functional form of the MTF does provide the highest values of explained variance by a significant margin. The Fourier method used here for image coregistration is able to detect and correct for shifts of the HRVIS images relative to the LRES images, and is not limited to integer multiples of the pixel resolution. Fig. 6 shows histograms of the individual shift found, having a mean value of 0.06 ± 0.10 in South and 0.36 ± 0.11 km in East direction. These values indicate a good coregistration accuracy of the satellite images after EUMETSAT's image rectification procedure. In consequence, not correcting for image misregistration reduces the correlation reported in Tab. 3 only slightly (NoCoReg). It can thus be argued that the additional complexity of coregistering the images is not worth the extra effort. For some extreme cases, however, the shift can vary by more than half a HRVIS pixel, and the coregistration procedure can prevent a degradation of accuracy.

5 Conclusions and Outlook

In this paper, a downscaling algorithm is presented to enhance the spatial resolution of Meteosat SEVIRI 0.6 and 0.8 micron narrowband images by a factor of 3. Our algorithm utilizes the broadband HRVIS channel in a linear model to resolve the high-frequency spatial variability for the lower spatial resolution narrowband channels. In addition, the spatial response functions of the SEVIRI channels are accounted for by an explicit convolution with the sensor modulation transfer function and the Fourier shift theorem

is used to coregister the HRVIS broadband channel to the narrowband channels.

The results of our uncertainty analysis reveal that our approach resolves high-frequency variability in the narrowband channels with an explained variance of 98.2% and 95.3% in the 0.6 and 0.8 micron channels, respectively, corresponding to residual standard deviations of 0.007 and 0.011 for the downscaled narrowband reflectances. In comparison, average values of 0.049 and 0.052 are expected as standard deviation between the reflectance of a HRES and an enclosing LRES pixel, variability which is completely neglected in the lower resolution narrowband images. These numbers support that the algorithm is able to provide physically consistent 0.6 and 0.8 micron reflectance images at the spatial resolution of the HRVIS channel.

Two sources of uncertainty of the proposed algorithm have been identified. First, it is assumed that the reflectance of the HRVIS channel is a linear combination of the 0.6 and the 0.8 micron reflectance. Second, the accuracy of the inversion of this linear relation relies on the correlation between the 0.6 and 0.8 micron channel reflectance, and the ratio of their variance. The latter uncertainty has been found to dominate, and is larger for the 0.8 micron channel, as its contribution to the HRVIS reflectance is less than that of the 0.6 micron channel. This fact is also reflected by the lower value of explained variance of the downscaled 0.8 micron channel given above.

Two aspects relevant to the accuracy of the downscaling algorithm have been studied in this paper. First, the correspondence of spatial variations between the narrowband and downsampled HRVIS channels improves significantly if the modulation transfer function of the SEVIRI sensors is explicitly used in the down-sampling procedure. Second, the coregistration of the HRVIS and narrowband channels has been quantified, and only a minor shift has been found of 0.06 ± 0.10 and 0.36 ± 0.11 km in South and East direction, respectively. Methods based on the discrete Fourier transform have been introduced to address both aspects.

During daylight hours, the presented downscaling algorithm provides important additional information for the narrowband observations that fall within the field of view of the HRVIS channel. In the future, we intend to apply this algorithm to reduce the

resolution mismatch between cloud products estimated from geostationary and polar-orbiting satellite platforms, which introduces biases in retrievals of cloud properties (Deneke et al., 2009b), as well as cloud radiative forcing (Oreopoulos et al., 2009). Other applications, such as the early detection of convective activity and the retrieval of land surface properties, can likely also benefit from the enhanced spatial resolution of the narrowband channels.

The main limitation of the approach in its current form is the fact that only a single linear model is used to downscale the entire SEVIRI scene. Since clouds dominate the spatial variations in reflectance (Deneke et al., 2009a) they also dominate the spectral variations and correlations in reflectance, and thus the applicability of the linear model. The relationship between narrowband and broadband radiances is known to be dependent on scene type (Li and Leighton, 1992). The use of scene-dependent linear models, using a previous pixel classification, could be a promising algorithm extension. Another promising extension could be the use of external sources of information within the downscaling process. For example, MODIS products could provide some of the required statistical parameters at high-resolution, such as the correlation between the 0.6 and 0.8 micron channel.

The algorithm presented in this paper is a physical downscaling method, which exploits the availability of higher spatial resolution information from the HRVIS channel as predictor (see Liu and Pu (2008) for the distinction between statistical and physical downscaling methods). The combination with statistical techniques could help extend the downscaling to additional SEVIRI spectral channels. It also needs consideration that the HRVIS channel is only available for part of the disk of the earth observed by SEVIRI, and that it still has a lower resolution than comparable polar-orbiting satellite imagers. Moreover, Deneke et al. (2009b) showed that biases in satellite-estimated cloud climatologies can also be reduced by using estimates of the unresolved variance. Alternatively or complementary, these biases may also be reduced by using approaches that simulate realistic surrogate variability at sub-pixel scale (see e.g., Venema et al., 2009; Schutgens and Roebeling, 2009).

Finally, our results demonstrate the potential of combining satellite images with different spatial and spectral resolution, to benefit from their individual strengths. This point will become even more important in the future for Meteosat Third Generation, which will acquire images with several different spatial resolutions.

5 Appendix A

Spectral Channel Characteristics

The following quantities are introduced to characterize the spectral response function η of a satellite detector. η is assumed to be normalized to a maximum value of unity here. The spectral width $\delta\lambda$ of a channel is given by

$$\delta\lambda = \int_0^{\infty} \eta(\lambda) d\lambda. \quad (\text{A1})$$

Then, the central wavelength λ_C can be defined as

$$\lambda_C = \frac{1}{\delta\lambda} \int_0^{\infty} \lambda \eta(\lambda) d\lambda. \quad (\text{A2})$$

The band-averaged extraterrestrial solar spectral irradiance ϕ_C of a channel is finally calculated by

$$\phi_C = \frac{1}{\delta\lambda} \int_0^{\infty} \phi(\lambda) \eta(\lambda) d\lambda. \quad (\text{A3})$$

Here, ϕ is the extraterrestrial solar spectrum at a sun-earth distance of 1 astronomical units.

The quantities λ_C and $\delta\lambda$ are well-suited to determine bulk optical properties of a medium illuminated by a spectrally constant source of irradiance. In case of the earth's atmosphere, however, the incident solar irradiance varies strongly with wavelength. It

is therefore more appropriate to use the product $\eta^* = \eta\phi$ of spectral response and solar spectrum instead of η to weight the reflection and transmission properties of the earth's atmosphere and surface for a spectral interval. Replacing η with η^* in Eq.A1 and Eq.A2, analogous quantities λ_C^* and $\delta\lambda^*$ can be obtained.

5 Appendix B

Statistical Inversion

This appendix presents general statistical relations used by this paper, and applies them in order to invert Eq.5. First, we consider a random variable y which is assumed to be linearly related to an independent variables x by

$$y = ax + b. \quad (\text{B1})$$

Here, a denotes the slope and b the offset of the linear model. Using standard definitions of variance and covariance, an estimate \hat{a} of the slope of the linear relation is given by

$$\hat{a} = \frac{\text{Cov}(x, y)}{\text{Var}(x)} = \text{Cor}(x, y) \sqrt{\frac{\text{Var}(y)}{\text{Var}(x)}}, \quad (\text{B2})$$

which minimizes the sum of the squared deviations of y from the linear equation. In the second equality, the linear correlation coefficient has been used, which is related to the covariance through

$$\text{Cor}(x, y) = \frac{\text{Cov}(x, y)}{\sqrt{\text{Var}(x) \text{Var}(y)}}. \quad (\text{B3})$$

The standard deviation σ_y of the difference between modeled and observed values can be calculated by

$$\sigma_y = \sqrt{\text{Var}(y) [1 - \text{Cor}(x, y)^2]}. \quad (\text{B4})$$

This equation also motivates the name *explained variance* $EV(x, y)$ for the square of $Cor(x, y)$, as $\frac{\sigma_x^2}{Var(y)}$ specifies the fraction of variance not explained by the linear model.

We now consider the downscaling problem discussed in this paper. Here, y depends linearly on two random and correlated variables x_1 and x_2 without any offset

$$y = a x_1 + b x_2. \quad (B5)$$

We are interested in the inversion of this linear model, to estimate x_1 and x_2 from y . Eq.B2 can provide the slope $S(x_1)$ of the least-squares solution for predicting x_1 from y . Inserting Eq.B5 into Eq.B2, and simplifying with general properties of covariance and variance, we obtain:

$$\begin{aligned} S(x_1) &= \frac{Cov(x_1, y)}{Var(y)} \\ &= \frac{1 + k Cor(x_1, x_2)}{a [1 + k^2 + 2 k Cor(x_1, x_2)]}, \end{aligned} \quad (B6)$$

with k given by

$$k = \sqrt{\frac{a^2 Var(x_2)}{b^2 Var(x_1)}}. \quad (B7)$$

As measure of the accuracy of this linear model, the explained variance $EV(x_1, y)$ of x_1 given y is used. We obtain

$$\begin{aligned} EV(y, x_1) &= \frac{Cov(y, x_1)^2}{Var(y) Var(x_1)} \\ &= \frac{[1 + k Cor(x_1, x_2)]^2}{1 + k^2 + 2 k Cor(x_1, x_2)}. \end{aligned} \quad (B8)$$

These results show that both the slope and the explained variance of the inversion depend only on the correlation of x_1 and x_2 , the slopes a and b , as well as the ratio of the variances of x_1 and x_2 . To apply these general results to the purposes of this paper, a , b , x_1 and x_2 have to be chosen appropriately.

Acknowledgements. The work of the first author has been funded through a EUMETSAT research fellowship. The authors would like to thank Wouter Greuell Jan Fokke Meirink and Victor Venema for their helpful comments and suggestions on earlier versions of this manuscript.

References

- 5 Anuta, P.: Spatial registration of multispectral and multitemporal digital imagery Using fast Fourier transform techniques, *IEEE Transactions on Geoscience Electronics*, 8(4), 353–368, 1970.
- Cros, S., Albuissou, M., and Wald, L.: Simulating Meteosat-7 broadband radiances using two visible channels of Meteosat-8, *Solar Energy*, 80(3), 361–367, 2006.
- 10 Deneke, H., Feijt, A., Lammeren, A., and Simmer, C.: Validation of a Physical Retrieval Scheme of Solar Surface Irradiances from Narrowband Satellite Radiances, *Journal of Applied Meteorology*, 44(9), 1453–1466, 2005.
- Deneke, H., Feijt, A., and Roebeling, R.: Estimating surface solar irradiance from METEOSAT SEVIRI-derived cloud properties, *Remote Sensing of Environment*, 112, 3131–3141, 2008.
- 15 Deneke, H., Knap, W., and Simmer, C.: Multiresolution analysis of the temporal variance and correlation of transmittance and reflectance of an atmospheric column, *Journal of Geophysical Research*, 2009a.
- Deneke, H., Roebeling, R., Wolters, E., Feijt, A., and Simmer, C.: On the Sensitivity of Satellite-Derived Cloud Properties To Sensor Resolution and Broken Clouds, in: *Current problems in atmospheric radiation: Proceedings of the International Radiation Symposium (IRS 2008)*, vol. 1100, pp. 376–379, 2009b.
- 20 Dürr, B. and Zelenka, A.: Deriving surface global irradiance over the Alpine region from Meteosat Second Generation by supplementing the HELIOSAT method, *International Journal of Remote Sensing*, 2008.
- 25 Dürr, B., Zelenka, A., Müller, R., and Philipona, R.: Verification of CM-SAF and MeteoSwiss satellite based retrievals of surface shortwave irradiance over the Alpine region, *International Journal of Remote Sensing*, 2009.
- EUMETSAT: SEVIRI Modulation Transfer Function (MTF) characterisations for MSG-1, MSG-2 and MSG-3, Tech. rep., EUMETSAT, Darmstadt, Germany, http://www.eumetsat.int/groups/ops/documents/file/zip_msg_mod_transf_fun_chars.zip, 2006a.
- 30

EUMETSAT: MSG SEVIRI spectral response characterization, Tech. rep., EUMETSAT, Darmstadt, Germany, http://www.eumetsat.int/groups/ops/documents/file/zip_msg_seviri_spec_res_char.zip, 2006b.

5 Greuell, W. and Roebeling, R.: Towards a standard procedure for validation of satellite-derived cloud liquid water path, *JAS*, 2009.

Gueymard, C.: The Sun's total and spectral irradiance for solar energy applications and solar radiation models, *Solar Energy*, 76(4), 423–452, 2004.

Harris, F.: On the use of windows for harmonic analysis with the discrete Fourier transform, *Proc. of the IEEE*, 66(1), 51–83, 1978.

10 Heidinger, A. and Stephens, G.: Molecular line absorption in a scattering atmosphere. Part III: Pathlength characteristics and effects of spatially heterogeneous clouds, *Journal of the Atmospheric Sciences*, 59(10), 1641–1654, 2001.

Jacobowitz, H., Stowe, L., Ohring, G., Heidinger, A., Knapp, K., and Nalli, N.: The Advanced Very High Resolution Radiometer Pathfinder Atmosphere (PATMOS) climate dataset: a resource for climate research, *Bulletin of the American Meteorological Society*, 84, 785–793, 2003.

Klüser, L., Rosenfeld, D., Macke, A., and Holzer-Popp, T.: Observations of shallow convective clouds generated by solar heating of dark smoke plumes, *Atmospheric Chemistry and Physics*, 8(10), 2833–2840, 2008.

20 Knap, W., Stammes, P., and Koelemeijer, R.: Cloud thermodynamic phase determination from near-infrared spectra of reflected sunlight, *Journal of the Atmospheric Sciences*, 59(1), 83–96, 2002.

Lensky, I. and Rosenfeld, D.: Clouds-aerosols-precipitation analysis tool (CAPSAT), *Atmospheric Chemistry and Physics*, 83, 6739–6753, 2008.

25 Li, Z. and Leighton, H.: Narrowband to broadband conversion with spatially autocorrelated reflectance measurements, *Journal of Applied Meteorology*, 31, 421–330, 1992.

Liu, D. and Pu, R.: Downscaling thermal infrared radiance for subpixel land surface temperature retrieval, *Sensors*, 8(4), 2695–2706, 2008.

30 Markham, B.: The Landsat sensor's spatial response, *IEEE Transactions on Geoscience and Remote Sensing*, GE-23(6), 864–875, 1985.

Müller, R., Matsoukas, C., Gratzki, A., Behr, H., and Hollmann, R.: The CM-SAF operational scheme for the satellite based retrieval of solar surface irradiance - A LUT based eigenvector hybrid approach, *Remote Sensing of Environment*, 113(5), 1012–1024, 2009.

- Oreopoulos, L. and Davies, R.: Plane parallel albedo biases from satellite observations. Part I: Dependence on resolution and other factors, *Journal of Climate*, 11, 919–932, 1998.
- Oreopoulos, L., Platnick, S., Hong, G., Yang, P., and Cahalan, R.: The shortwave radiative forcing bias of liquid and ice clouds from MODIS observations, *Atmospheric Chemistry and Physics Discussions*, 9, 10 337–10 366, 2009.
- Platnick, S., King, M., Ackerman, S., Menzel, W., Baum, B., Riedi, J., and Frey, R.: The MODIS cloud products: algorithms and examples from Terra, *IEEE Transactions on Geoscience and Remote Sensing*, 44(2), 459–473, 2003.
- Roebeling, R. and van Meijgaard, E.: Evaluation of the daylight cycle of model predicted cloud amount and condensed water path over Europe with observations from MSG-SEVIRI, *Journal of Climate*, 22, 1749–1766, 2008.
- Roebeling, R., Deneke, H., and Feijt, A.: Validation of cloud liquid water path retrievals from SEVIRI using one year of CloudNET observations, *Journal of Applied Meteorology*, 47(1), 206–222, 2008.
- Rossow, W. and Schiffer, R.: ISCCP cloud data products, *Bulletin of the American Meteorological Society*, 71, 2–20, 1991.
- Schmetz, J., Mhita, M., and van den Berg, L.: METEOSAT Observations of Longwave Cloud-Radiative Forcing for April 1985, *Journal of Climate*, 3, 784–791, 1990.
- Schmetz, J., Pili, P., Tjemkes, S., Just, D., Kerkmann, J., Rota, S., and Ratier, A.: An introduction to Meteosat Second Generation (MSG), *Bulletin of the American Meteorological Society*, 83, 977–992, 2002.
- Schulz, J., Albert, P., Behr, H.-D., Caprion, D., Deneke, H., Dewitte, S., Dürr, B., Fuchs, P., Gratzki, A., Hechler, P., Hollmann, R., Johnston, S., Karlsson, K.-G., Manninen, T., Müller, R., Reuter, M., Riihelä, A., Roebeling, R., Selbach, N., Tetzlaff, A., Thomas, W., Werscheck, M., Wolters, E., and Zelenka, A.: Operational climate monitoring from space: the EUMETSAT satellite application facility on climate monitoring (CM-SAF), *Atmospheric Chemistry and Physics*, 9(5), 1687–1709, 2009.
- Schutgens, N. and Roebeling, R.: Validating the validation: the influence of liquid water distribution in clouds on the intercomparison of satellite and surface observations, *Journal of Atmosphere and Ocean Technology*, 1, 1–2, 2009.
- Stephens, G. and Kummerow, C.: The remote sensing of clouds and precipitation from space: a review, *Journal of the Atmospheric Sciences*, 64, 3742–3765, 2007.
- Venema, V., Garcia, S., and Simmer, C.: A new algorithm for the downscaling of 3-dimensional

- cloud fields, submitted to Quarterly Journal of the Royal Meteorological Society, 2009.
- Walker, P. and Mallawaarachchi, T.: Disaggregating agricultural statistics Using NOAA-AVHRR NDVI - a variant of the traditional spatial problem, Remote Sensing of Environment, 63(2), 112–125, 1998.
- 5 Wielicki, B., Barkstrom, B., Harrison, E., III, R. L., Smith, G., and Cooper, J.: Clouds and the Earth's Radiant Energy System (CERES): An Earth Observing System experiment, Bulletin of the American Meteorological Society, 77(5), 853–868, 1995.
- Wolters, E., Deneke, H., van den Hurk, B., Meirink, J. F., and Roebeling, R.: Cloud Phase and Resolution, submitted to JGR, 2009.
- 10 Woods, J., Barkmann, W., and Horch, A.: Solar heating of the oceans - diurnal, seasonal and meridional variation, Quarterly Journal of the Royal Meteorological Society, 110(465), 633–656, 1984.

Meteosat	VIS006			VIS008			HRVIS		
	λ_0	$\delta\lambda$	ϕ_C	λ_0	$\delta\lambda$	ϕ_C	λ_0	$\delta\lambda$	ϕ_C
8	640.2	74.5	1594.8	809.3	57.3	1106.8	708.2	421.3	1395.6
9	640.3	73.4	1594.4	808.2	57.3	1109.6	706.4	422.2	1400.1
10	638.2	70.9	1601.3	808.2	57.0	1109.5	707.0	428.7	1398.9
	λ_0^*	$\delta\lambda^*$	-	λ_0^*	$\delta\lambda^*$	-	λ_0^*	$\delta\lambda^*$	-
8	639.0	73.7	-	808.6	54.6	-	669.7	388.6	-
9	639.1	72.5	-	807.4	55.1	-	668.0	387.5	-
10	637.0	70.3	-	807.5	54.4	-	668.2	385.0	-

Table 1. Central wavelength λ_0 , channel width $\delta\lambda$ (both in nm), and band-averaged extraterrestrial solar spectral irradiance ϕ_C ($W/m^2/\mu m$) at a sun-earth distance of 1 astronomical units for the SEVIRI radiometers onboard the Meteosat-8 to 10 satellites and for the 0.6 micron, 0.8 micron (VIS008) and HRVIS channels, calculated from the spectral response functions provided by EUMETSAT (2006b) and the solar spectrum of Gueymard (2004). The central wavelength λ_0^* and channel width $\delta\lambda^*$ for the spectral response weighted by the solar spectrum are also listed.

	a	b	EV(Eq.5)	$S(r_{06})$	$S(r_{08})$	EV(r_{06})	EV(r_{08})	Cor(r_{06}, r_{08})
Mean	0.667	0.368	99.7	0.949	1.000	98.5	95.6	0.945
SDev	0.025	0.020	0.1	0.036	0.041	0.5	1.6	0.020

Table 2. Annually averaged parameters (Mean) and their standard deviation (SDev) obtained by the downscaling algorithm. This includes: the slopes a and b of Eq.5, and the explained variance EV(Eq.5) of the underlying linear equation; the slopes $S(r_{06})$ and $S(r_{08})$ used to scale high-frequency variations in the HRVIS channel to estimate unresolved variability in the 0.6 and 0.8 micron reflectance (based on Eq.B6); the explained variance EV(r_{06}), EV(r_{08}) of these estimates; and the correlation coefficient between variations in the 0.6 and 0.8 micron reflectance. Explained variances (EV) are listed in units of percent.

	Ref	LP48	3x3	1x1	5x5	NoCoReg
EV	99.68	99.08	99.04	96.83	94.60	99.61
SDev	0.11	0.28	0.27	0.94	2.32	0.14

Table 3. Effect of image coregistration and spatial averaging methods on the explained variance (EV) and its standard deviation (SDev) for the linear model of HRVIS, 0.6 and 0.8 micron reflectance expressed by Eq.5 and given in percent. For a description of the different methods, see the text.

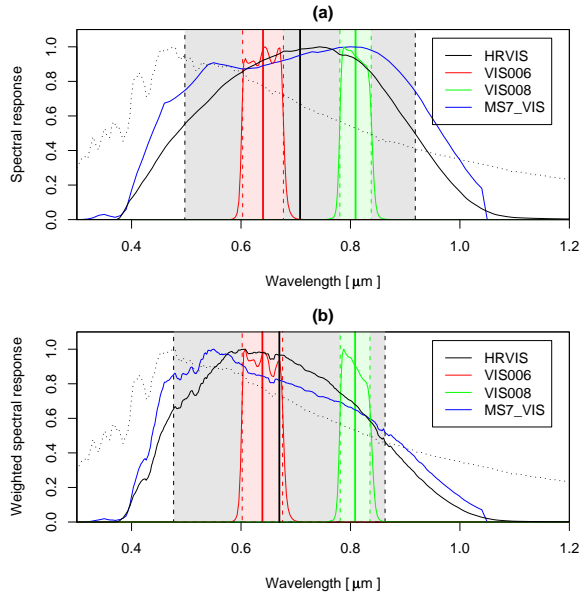


Fig. 1. Spectral response functions of the Meteosat-9 SEVIRI radiometer for the 0.6 micron (red), 0.8 micron (green) and HRVIS channel (black) (EUMETSAT, 2006b). The central wavelength of each channel is marked by a thick colored line, and the spectral region covered by the channel width has been shaded. The response of the Meteosat-7 MVIRI solar channel is also included for comparison (blue). The normalized spectral response functions are plotted in (a), while the spectral response functions weighted by the solar spectrum of Gueymard (2004) are displayed in (b). The solar spectrum is added as dotted line to both plots.

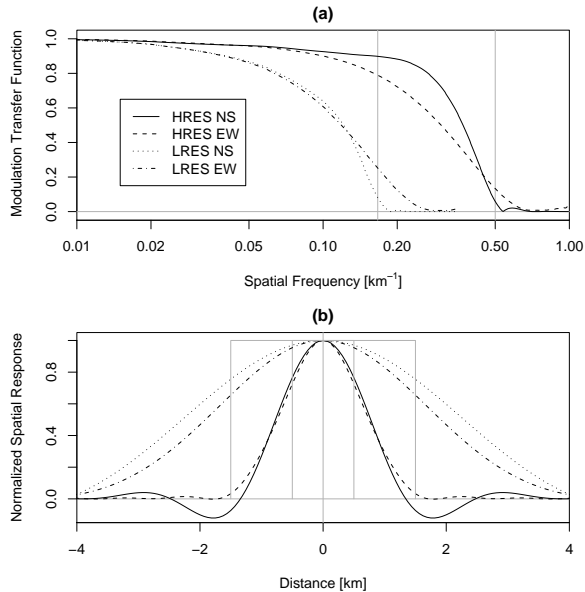


Fig. 2. (a) Modulation transfer function (MTF) of the $3 \times 3 \text{ km}^2$ low-resolution(LRES) 0.6 and $0.8 \mu\text{m}$ channels and the res1 high-resolution visible channel (HRES) for Meteosat-9 in North-South (NS) and East-West (EW) directions (EUMETSAT, 2006a). The Nyquist frequencies corresponding to the sampling resolution are shown in grey, with values of $\frac{1}{6} \text{ km}^{-1}$ (LRES) and $\frac{1}{2} \text{ km}^{-1}$ (HRES). (b) Point spread function of the SEVIRI detectors reconstructed from the MTFs (see text for details), as a function of distance from the pixel center. In grey, a perfect step response at LRES and HRES sampling resolution is also shown.

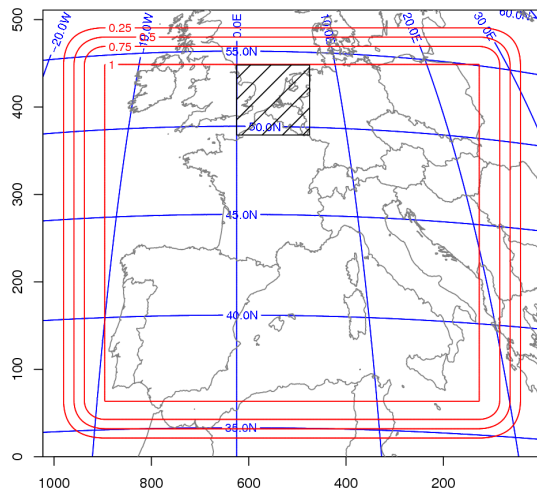


Fig. 3. Region of the SEVIRI field of view used for this paper, consisting of 1024×512 pixels. Also shown are contours of latitude and longitude in blue, and of the amplitude of the window function used for Fourier analysis in red. The subregion shown in Fig. 4 is marked by a black shaded rectangle.

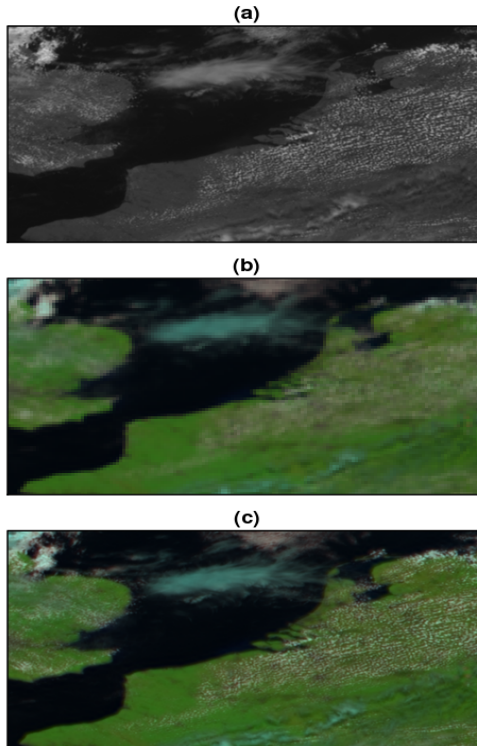


Fig. 4. Example output of the downscaling algorithm in comparison to standard SEVIRI images, based on a scene from June 26th 2008 of England, the British channel, north-eastern France, Belgium and the Netherlands. Panel (a) shows the HRVIS reflectance in grey levels, while (b) shows the *day natural colors* RGB composite of Lensky and Rosenfeld (2008) at standard SEVIRI resolution. Panel (c) is based on the downscaled 0.6 and 0.8 micron reflectances at HRVIS channel resolution, combined with an 1.6 micron image obtained by trigonometric interpolation.

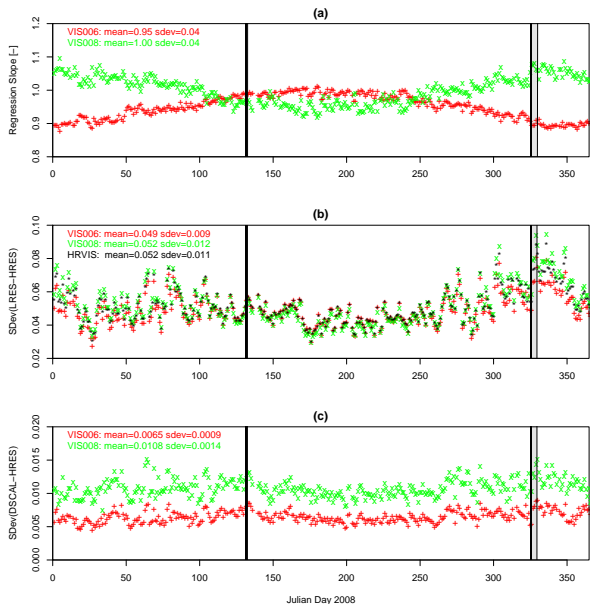


Fig. 5. Annual time series of (a) the linear regression slopes found to link variations in the HRVIS channel to unresolved variations in the 0.6 (VIS006, red) and 0.8 micron (VIS008, green) channel; (b) the estimated standard deviation of the difference between 1×1 (HRES) and $3 \times 3 \text{ km}^2$ (LRES) images for the three spectral channels; and of (c) the estimated residual standard deviation of the proposed downscaling algorithm. Periods when Meteosat-8 replaced Meteosat-9 as operational satellite due to spacecraft anomalies have been shaded in grey.

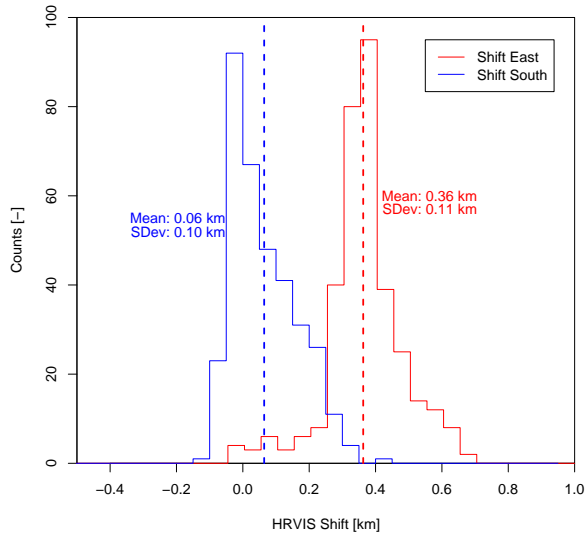


Fig. 6. Histogram of the shifts of the HRVIS image relative to the 0.6 and 0.8 micron channel in Northern and Eastern direction, obtained for 345 Meteosat-9 scenes from 2008. The shift of the images is expressed as distance at the nadir point of the satellite in kilometers (km).